



Universiteit
Leiden
The Netherlands

Optical coherence tomography for coronary artery disease : analysis and applications

Liu, S.

Citation

Liu, S. (2018, September 4). *Optical coherence tomography for coronary artery disease : analysis and applications*. Retrieved from <https://hdl.handle.net/1887/64938>

Version: Not Applicable (or Unknown)

License: [Licence agreement concerning inclusion of doctoral thesis in the Institutional Repository of the University of Leiden](#)

Downloaded from: <https://hdl.handle.net/1887/64938>

Note: To cite this publication please use the final published version (if applicable).

Cover Page



Universiteit Leiden



The handle <http://hdl.handle.net/1887/64938> holds various files of this Leiden University dissertation.

Author: Liu, S.

Title: Optical coherence tomography for coronary artery disease : analysis and applications

Issue Date: 2018-09-04

HISTOGRAM-BASED STANDARDIZATION OF INTRAVASCULAR OPTICAL COHERENCE TOMOGRAPHY IMAGES ACQUIRED FROM DIFFERENT IMAGING SYSTEMS

Abstract — Intravascular optical coherence tomography is widely used for analysis of the coronary artery disease. Its high spatial resolution allows for visualization of arterial tissue components in detail. There are different systems on the market, each of which produces data characterized by its own intensity range and distribution. This limits the comparison of the results, especially when intensity values are used. In order to overcome the difference in the intensity range and distribution, we developed an intensity mapping framework to match intensities based on an exact histogram matching technique. Experiments were performed with aligned data from systems of the two major vendors, St.Jude and Terumo. A leave-one-out cross validation was used to compare the global and local schemes for the determination of the target histograms. Our results show that: 1) The intensities can be matched well with good generalization, and 2) Even though the local scheme marginally outperforms the global scheme, the latter is better suited for practical usage.

This chapter is based a submitted manuscript: S. Liu, O. Dzyubachyk, J. Eggermont, S. Nakatani, B. P. F. Lelieveldt, and J. Dijkstra, **Histogram-Based Standardization of Intravascular Optical Coherence Tomography Images Acquired from Different Imaging Systems**, *Med. Phys.*, Accepted for publication.

4.1 Introduction

Cardiovascular diseases (CVDs) are the leading cause of death worldwide [31]. Introduction of intravascular optical coherence tomography (IVOCT) has largely advanced understanding and treatment of one of the most common CVDs, the coronary artery disease [5, 14, 8, 15]. Design of IVOCT enables visualization of superficial tissue structures of the arteries with resolution as high as 5–10 μm . The wavelength of its light source is around 1300 nm, which permits a relatively deep penetration into the vessel wall. The *intravascular* term indicates that the images are acquired from the inside of the blood vessel. For current commercial systems, this is achieved by inserting a catheter into the coronary artery, pushing away the blood by injecting a flush media and pulling it back through the lesion location. The catheter has been designed to emit near-infrared light towards the artery wall and to receive the back-propagated light. The received light is recorded as a one-dimensional signal (A-line) containing the back-propagated intensities ordered by ascending distances to the catheter. By rotating the catheter tip with a constant speed, two-dimensional images can be generated. Centering at the catheter, each cross-sectional image contains about 500 A-lines from different directions. These A-lines are recorded as a raw image in polar coordinates, as shown in Fig. 4.1(b,e), or transformed into the Cartesian coordinates, as shown in Fig. 4.1(c,f). As the catheter is pulled back at a constant speed using a motorized pullback device, a stack of images, referred to as a *pullback* is acquired.

The use of IVOCT in clinical studies increases exponentially [15]. Because of its high resolution, IVOCT contributed to confirmation of pathological findings on progression of (neo)atherosclerosis by visualizing morphologies like intimal erosion, fibrous plaque, calcified nodule, lipid pool, macrophages distribution, intraluminal thrombus, etc. [95, 4, 96, 97, 98, 99, 100]. Attracted by the conspicuous clinical prospects, many efforts were paid to detection and characterization of IVOCT morphologies, such as fibrous, lipid-rich and calcified plaques [18], macrophages distributions [95], thrombus [101], side-branches [102, 103], struts [104, 105, 44] and struts embedding [106] with image intensities, and/or optical parameters [28, 40]. However, diversity of IVOCT data can limit comparison of the results, especially when intensity values are used. In particular, there is no consented standard for the imaging range, unlike e.g. in computed tomography (CT), meaning that IVOCT images generated with different commercially available systems are typically characterized by different intensity ranges. The most commonly used commercial systems are Illumien Optis from St. Jude Medical (St. Paul, MN, USA), which saves the raw data in a 16-bit format, and Lunawave from Terumo (Tokyo, Japan), which saves the raw data in a 8-bit format.

As a concrete example, the Cartesian images from these two systems are shown in Fig. 4.1(c,f), and their polar counterparts are shown in Fig. 4.1(b,e). Images were acquired shortly after each other during the same intervention at the same location inside an artery of one patient. The histograms of the corresponding regions on the IVOCT images acquired by the two systems

indicate different intensity ranges within the same tissue type. Furthermore, different shape of these histograms suggests that relationship of intensities between these two systems is not simply linear. In fact, an exponential relationship has been observed in our previous work [88].

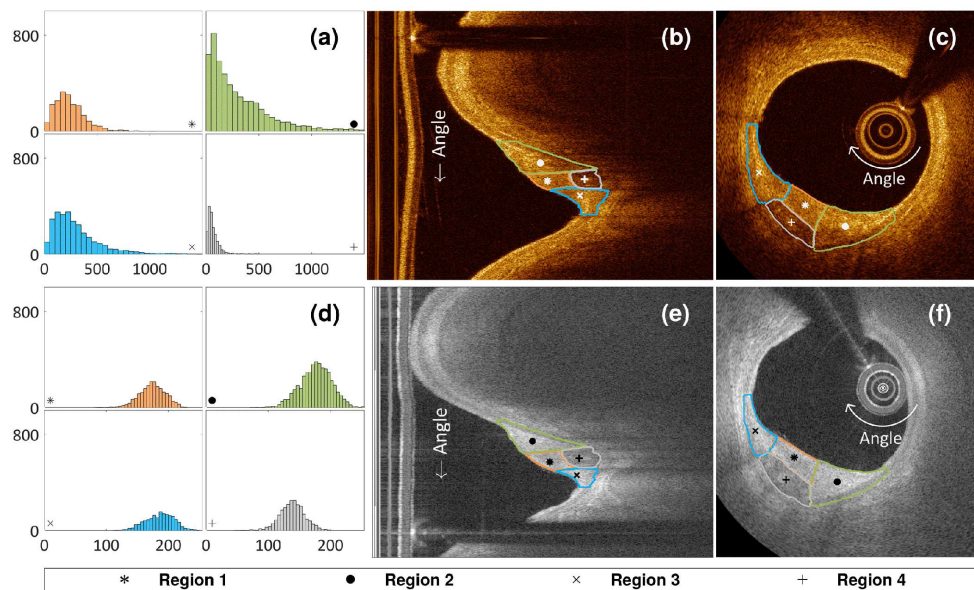


Figure 4.1: Histograms (a) of regions delineated in St.Jude polar (b) and Cartesian (c) images. Histograms (d) of regions delineated in Terumo polar (e) and Cartesian (f) images. Side-branches and lesions were used as landmarks to find the corresponding locations in St.Jude and Terumo images. Regions were separated according to their morphological appearance and visible borders and are correspondingly delineated in the polar images. Delineated regions on both polar and Cartesian images and the corresponding histogram bars are shown using the same colors.

Most OCT studies used the same type of IVOCT system to guarantee high reproducibility. On the other hand, doing so limits the scope of developed applications: when the same method is applied to data from another vendor that has different intensity distribution, repeated validation is required. To improve efficiency of development, images need to be standardized across devices. Only few papers on this topic have been published in the IVOCT field, whereas several papers on increasing the comparability of ophthalmological OCT images were published. In particular, a normalization approach was proposed for comparing images from two vendors [107]. This approach involves three steps: density scaling and sampling, noise reduction, and amplitude normalization. It was later improved by integrating virtual averaging [108]. This A-line normalization approach was shown to reduce the measurement difference [109] and the appearance disparity [110].

In this work, we explore the possibility of converting the data between different OCT systems and propose a matching scheme with good generalization and minimal loss of detail. Our pretrained algorithm can also be used for intensity matching when the target data is not given. By doing this, when a method developed for data acquired with system-A needs to be evaluated with data acquired with system-B, we can modify the data from system-B to follow the intensity distribution of system-A, such that the method can be tested on the data from system-B with minimum modification. Such data conversion is referred to as the *histogram modification* [111, 112, 113, 114]. The basic histogram matching theory has been proposed in the work of Hummel et al. [111]. Since then, this study has been widely used as the fundamental theory in image modification studies at the histogram level. Later, the exact histogram specification (EHS) was proposed as a successful discrete solution to the model in practice [112, 113, 114]. This approach was used to produce comparable measurements in ophthalmological OCT images generated with low signal strength to that generated with high signal strength [115] and to compensate light attenuation in confocal microscopy [116].

Our main goal in this paper is to propose a framework for matching intensities in OCT images from different vendors using EHS. A straightforward approach would be to match intensities per pullback. We compare this *global* scheme to a *local* scheme that takes the local intensity variations into the consideration. All the analysis is conducted with raw polar images, whereas the Cartesian images are only used for the visualization of results. The *in vivo* patient data used in this study is unique in the sense that both St.Jude and Terumo pullbacks were specially acquired for this study. More elaborate explanation of this is provided further in the manuscript.

The paper is structured as follows. For better understanding of the underlying principles and terminology, we explain both the model and the EHS in Section 4.2. In Section 4.3, the data and its processing are described, the distance measures are introduced, and the matching schemes are proposed and validated. Results are reported and discussed in Section 4.4 to Section 4.6. Finally, in Section 4.7 we draw the conclusions.

4.2 Theory and terminology

Each 2-D image can be represented as a matrix $I(x, y)$, which is the discrete subsample of a bounded surface function $f(x, y)$, where $\{(x, y) \mid 0 \leq x \leq N, 0 \leq y \leq M\}$. The intensity function $f(x, y)$ follows a distribution function $P_f(t)$ that indicates the chance of $f(x, y)$ being less or equal than t . Given two images $f_s \sim P_{f_s}(z_s)$ and $f_t \sim P_{f_t}(z_t)$, the goal of histogram transformation is to search for a mapping T such that composition $T \circ f_s \sim P_{f_t}(z_t)$. In this work, f_s and f_t are referred to as the source and the target image, respectively. This search has been formulated by Hummel et al.

[111] as an optimization problem:

$$\hat{T} = \arg \min_T \int_{a_1}^{a_2} [p_{T \circ f_s}(z) - p_{f_t}(z)]^2 dz, \quad (4.1)$$

where $[a_1, a_2]$ defines the range of image intensities. Here $p_X(z)$ is the probability density function (*pdf*) of image X , which is the derivative of the distribution function $P_X(z)$, and z is intensity level.

A unique monotonic solution of this model was given in [111]:

$$\tilde{T}(z_s) = P_{f_t}^{-1}(P_{f_s}(z_s)), \quad p_{f_s}(z_s) > 0, \quad \text{for } \forall z_s. \quad (4.2)$$

In practice, p_X in both source and target spaces is usually estimated as the normalized histogram vector: $p_X = \{p_i \mid \sum p_i = 1, i \in \{0, \dots, 2^{L_0} - 1\}\}$, where L_0 denotes the maximum gray level of the images, p_i denotes the frequency of the image intensity corresponding to the interval $[z_i, z_{i+1})$. Conventionally, the interval is referred to as a *bin*; $\{z_i\}$ are the bin edges; the average of every two adjacent bin edges $c_i = (z_i + z_{i+1})/2$ is the bin center, and p_i is the bin value. We define the bin edges for the i th bin as $[c_i - 0.5, c_i + 0.5)$ in this work.

To ensure that the distribution function P_X is monotonically increasing, the following approximation is used:

$$P_j = \frac{c_j - z_j}{z_{j+1} - z_j} p_j + \sum_{i=0}^{j-1} p_i. \quad (4.3)$$

This approximation is equivalent to interpolating $P_j(z)$ for $z \in [z_j, z_{j+1})$ with a piecewise-linear function, the slope of which is p_j and the intercept is $\sum_{i=0}^{j-1} p_i$. Using this monotonic approximation, \tilde{T} can be estimated with Eq. 4.2. However, this estimation only shifts bins centers, and splitting of bins is not possible. This becomes especially problematic when the source and the target images are within different intensity range, such as e.g. transforming 8-bit images to 16-bit images or the other way around. Since the bins cannot be split, information can only be retained based on the image that is represented by less bins. Attempts have been made to include local information [111] (local mean, entropy, etc.) into the objective function as a “context-aware” term, but doing so introduces more parameters, and the transformed images tend to be blurred.

The aforementioned issues can be overcome by a technique called exact histogram specification (EHS) [113, 114, 112]. In the following, we will use the previously introduced notations. For an image of size $M \times N \times P$ with gray values in $\{0, 1, \dots, 2^{L_0} - 1\}$, the histogram divides $M \times N \times P$ pixels into 2^{L_0} bins. The fundamental idea behind EHS is to strictly order all the pixels, such that the ordered pixels can be divided according to any given target histogram. This usually cannot be done by using intensities only, thus auxiliary information needs to be introduced.

Local means and wavelet coefficients have been reported to be successful source of auxiliary information for achieving strict ordering [113, 114]. In a

more recent study [112], a moderately improved performance in nature images has been reported with a proposed auxiliary term involving three hyper-parameters. Compared to the other two aforementioned approaches, local-means approach better copes with noise and involves no hyper-parameters, thus it is chosen in this study as the noise level of OCT images is known to be high.

Considering the intensity at each pixel as the first scale of the local mean, for each pixel i we calculate a vector of multi-scale local means with increasing window size $\mu = [\mu_1(i), \mu_2(i), \dots, \mu_K(i)]$, K being the number of scales. Consequently, all the pixels in the image can be ordered lexicographically with a relational operator defined as:

$$\{i \prec j \mid \mu_\ell(i) = \mu_\ell(j) \forall \ell < \ell_0, \mu_{\ell_0}(i) < \mu_{\ell_0}(j)\}. \quad (4.4)$$

As result of using this approach, pixels in one image are expected to be ordered strictly by using just a few scales. It was observed that $K = 6$ scales are usually enough to arrange all the pixels in a strictly ascending order [113]. Once the strict ordering is achieved, the pixels can be easily grouped again following the histogram defined in the target image.

In practice, the EHS is often used to estimate the target image(s) given the source image(s) and the target histogram. In our case, however, the target histogram is unknown and should first be defined using a group of matched source and target images. Thus our task is two-fold: 1) To estimate the target histogram(s) from the matched images, and 2) To apply the estimated histogram(s) to a new source image. The following section describes our method in full detail.

4.3 Materials and methodology

As it was previously elaborated, the key step for using EHS is to define the target histogram.

4.3.1 Global and Local matching schemes

To determine the target histogram, the most straightforward approach is to use the overall histogram generated with all the images. However, using the global histogram as a reference might result in information loss as some of the less represented tissue structures might get overshadowed in the global histogram. Using local histograms might help resolving this issue.

Therefore, we introduce a *Global* scheme and a *Local* scheme for determination of the target histogram. For applying the Local scheme, each pullback is split into smaller sections (our pullback alignment and splitting algorithm is described in the following section). For providing a formal definition, we denote the database of matched histogram pairs as $\mathcal{H} = \{(H_1^k, H_2^k) \mid k = \overline{1, N_H}\}$, where H_1^k denotes the histogram of k^{th} section in

the original space (e.g. St.Jude), H_2^k denotes its counterpart in the target space (e.g. Terumo), and N_H is the size of the database.

For matching a given image with histogram H_1^* , the Global scheme uses one overall histogram as the target histogram, i.e.:

$$H_2^G = \sum_{k=1}^{N_H} H_2^k. \quad (4.5)$$

The Local scheme determines the target histogram for each section as the second component of the database entry whose first component is the most similar to H_1^* .

$$H_2^L = H_2^{\operatorname{argmin}_{k=1, \dots, N_H} d(H_1^*, H_1^k)}. \quad (4.6)$$

Here $d(H_i, H_j)$ denotes dissimilarity between two histograms H_i and H_j . The remainder of this section describes creation of the histogram database and introduces the dissimilarity measures.

4.3.2 Data description and alignment

In our case, the target histogram is estimated using a dataset of matched images. As the final goal of this study is to transform OCT images both from intensity space of St.Jude system (St.Jude space) to that of Terumo system (Terumo space) and the other way around, the target histograms in both St.Jude and Terumo spaces need to be determined. To achieve this, eight *in vivo* pullbacks were acquired from left anterior descending artery (LAD) of two different patients, marked as *A* and *B*. The data acquisition strictly followed the clinical guideline of Sakurabashi Watanabe Hospital (Osaka, Japan), and the analysts from Leiden University Medical Center (Leiden, The Netherlands) were blinded from all patients' information. For each patient, IVOCT pullbacks from the same vessel segment were acquired shortly after each other with St.Jude and Terumo systems, before and after the stent implanting procedure. As a result, four pairs of corresponding St.Jude–Terumo pullbacks were made available for the study. The St.Jude pullbacks were acquired at a pullback speed of 36 mm in 180 frames per second with a frame interval of 0.2 mm, and the Terumo pullbacks were acquired at a pullback speed of 40 mm in 158 frames per second with a frame interval of 0.25 mm. Raw polar images as provided by the vendors are used in this study. St.Jude images are 16-bit “linear” with a transversal pixel size of 0.0050 mm, and Terumo images are 8-bit “log-like” compressed with a transversal pixel size of 0.0049 mm.

Due to different distal and proximal locations in two corresponding pullbacks, images within overlapping part of the vessel should be matched. We determine the start and the end frames of overlapping part by searching for identical side-branches that are closest to the proximal and the distal parts of the pullbacks. Since we primarily aim at analyzing the tissue region, images with stent struts points are excluded (more elaborate discussion about this is provided in Section 4.6).

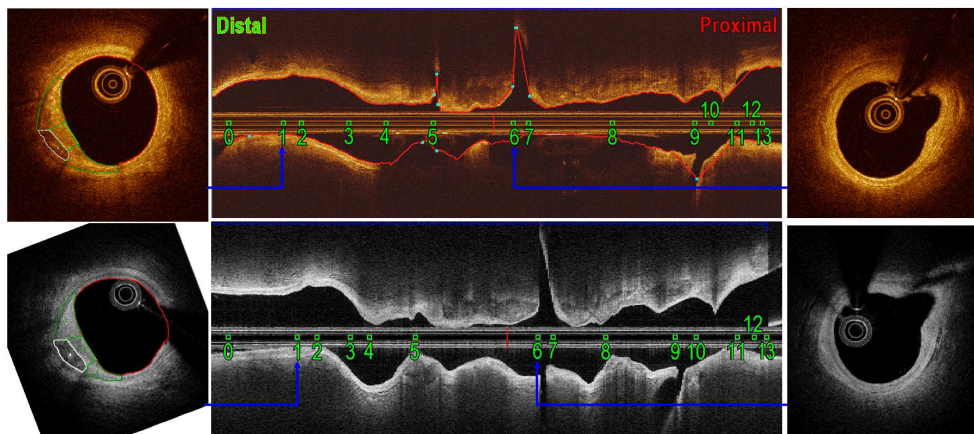


Figure 4.2: The landmarks for aligning the pullbacks.

Compared to the histogram of the entire overlapping part of pullbacks, histograms of smaller sections may preserve more local structural information. Therefore, we further split the overlapping part into small sections using key frames defined by two main types of anatomical landmarks (as shown in Fig. 4.2): the side-branches and the tissue types with identical patterns, e.g. culprit lesion visible in Fig. 4.1(c,f). For the post-stenting pullbacks, the proximal and distal edges of the stent struts are also considered to be crucial landmarks. Key frames were identified independently by two experienced IVOCT readers, using QCU-CMS (Quantitative Coronary Ultrasound—Clinical Measurement Systems; Leiden University Medical Center, Leiden, The Netherlands), which is the research version of QIVUS (Quantitative IntraVascular UltraSound; Medis, Leiden, The Netherlands). Only landmarks with consensus were selected.

Even though the catheter is pulled back with a uniform speed, the number of frames within a certain section can be affected by the heartbeat cycle, slight bending of the artery, interaction between the catheter and the artery wall, and so on. Due to this effect, finer splitting or frame-to-frame matching is not possible without introducing an interpolation error.

Table 4.1 gives an overview of the aligned data. Patient-A had no stent planted beforehand, while Patient-B did have one. Hence, the number of frames without stent struts in Patient-B is smaller than in Patient-A. Overall, the pullbacks were aligned with twenty-three key frames. Within these frames, regions of clinical interest (ROI) were delineated based on their appearance and visible borders according to the consensus [8]; see Fig.4.1. In total, we have eighteen corresponding pairs of sections and thirty-eight ROIs. After correspondence between the sections had been established, the database of matched histogram pairs was generated using foreground regions bounded by the lumen border and 1 mm behind. This corresponds to the depth of 200 pixels

Table 4.1: Data description

Patient	Treatment	St.Jude				Terumo				Landmark	Section	ROI
		PL ^a (mm)	All ^b	Max ^b	Min ^b	PL ^a (mm)	All ^b	Max ^b	Min ^b			
A	Pre-stenting	108	507	80	10	168	389	88	9	14	13	32
	Post-stenting	108	69	52	17	147	53	41	12	4	2	4
B	Pre-stenting	75	40	21	19	152	33	19	14	3	2	1
	Post-stenting	75	12	12	12	111	10	10	10	2	1	1
Total			628	80	10		485	88	9	23	18	38
ROI	Adventitia	Calcification			Fibrous		IML ^c	Lipid		Neointima		Total
No.	4	11			10		4	3		6		38

^aPL: total length of the entire pullback

^bAll, Max, and Min: the total, maximal, and the minimal numbers of frames in the aligned sections

^cIML: intima-media layer

in St.Jude polar image and 204 pixels in Terumo polar image. The lumen border is detected by the QCU-CMS software in an automated manner.

4.3.3 Dissimilarity between histograms

The Euclidean and the Kolmogorov-Smirnov distances are used for comparing two histograms. They are first used in the analysis of the local variations and, after that, for evaluation of matching schemes.

For calculating the distances, the histograms are normalized to obtain the probability density functions (*pdf*'s) and the corresponding cumulative density functions (*cdf*'s). The Euclidean distance for measuring dissimilarity between two *pdf*'s p and q is defined as:

$$d_{x2}(p, q) = (p - q) \cdot (p - q)', \quad (4.7)$$

the discrete approximation of which is equivalent to the objective function in Eq. 4.1. The Kolmogorov-Smirnov distance measures dissimilarity between the distribution functions (also known as *cdf*'s) P and Q :

$$d_{KS}(P, Q) = \max_i |P_i - Q_i|. \quad (4.8)$$

4.3.4 Validation

Leave-one-out validation is used to compare the Global and Local schemes. One of the four pullback pairs is left out in turn, and the target histogram is determined with the other three. Consequently, the intensities of the left-out pullback are matched. As part of each leave-one-out experiment, median intensities within each ROI are compared in both target and matched images. The target and matched median values are shown in the scatter plot and compared in the Bland-Altman plot. The scatter plot can show whether two groups of data are linearly related and how much the trend line deviates from the diagonal line, which is the ideal case indicating that two groups of data

match perfectly. The Bland-Altman plot shows the average versus the difference of each two compared values, which reveals the difference of two groups of data more explicitly. The mean and the standard deviation values of the difference are also called the systematic difference and the random error. With a properly low random error, the closer the systematic difference to zero level is, the more likely that two groups of data are originating from the same distribution. For reference, also the key frames are matched using the target histograms extracted directly from their corresponding aligned frames.

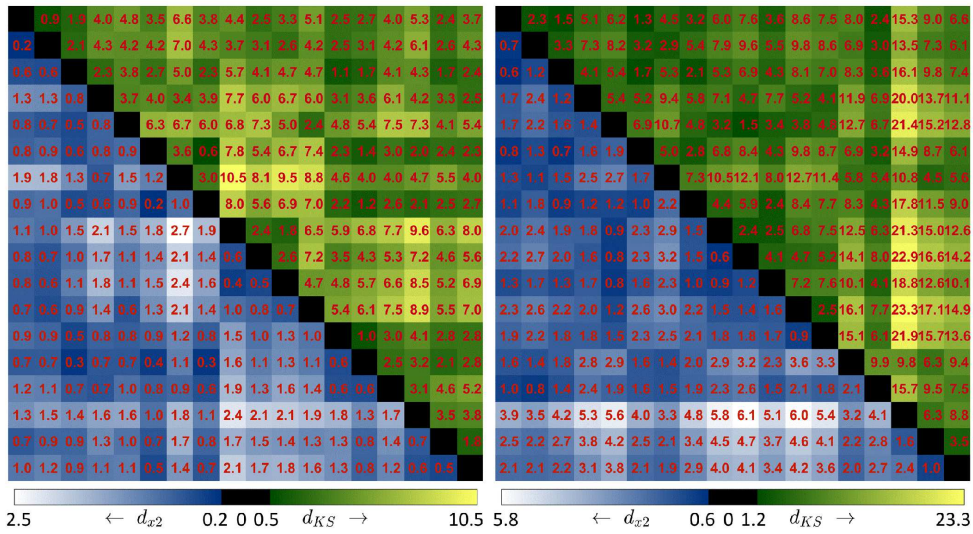


Figure 4.3: The distances between all the histograms in the database for St.Jude (left) and Terumo (right) spaces. All the distances were multiplied by a factor of 100 for presentation purposes. In each distance map, d_{x_2} and d_{KS} are shown in the lower and upper triangles, respectively.

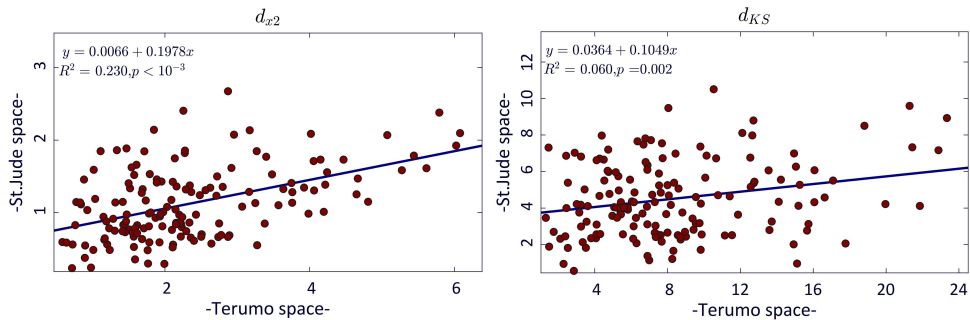


Figure 4.4: Linear regression of distances of all the histograms in our database for St.Jude and Terumo.

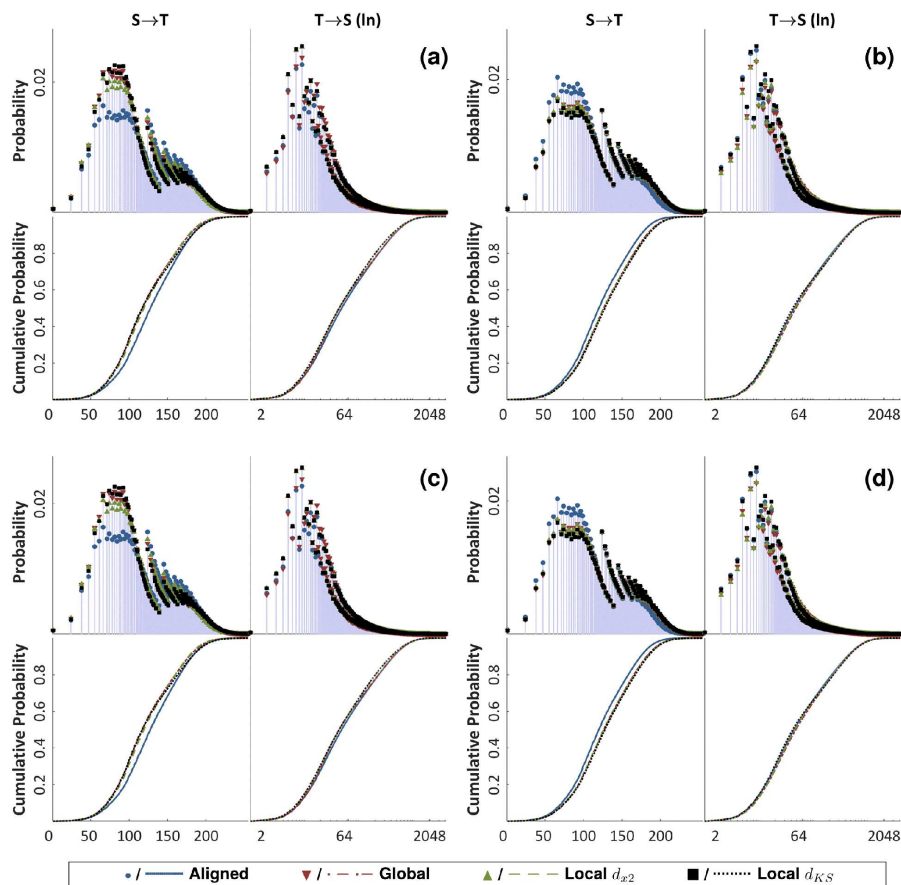


Figure 4.5: The aligned and trained probability and the cumulative probability distributions for leaving the 1st (a), the 2nd (b), the 3rd (c) and the 4th (d) pullback out. Target profiles for both St.Jude ($S \rightarrow T$) and Terumo ($T \rightarrow S$) images are shown. For the latter case, the x -axis is shown in the logarithm scale (\ln) for the sake of better visualization.

4.4 Results

We calculated the distances between all the histograms in two spaces. Figure 4.3 gives a general overview of all the dissimilarities. In the scatter plot of distances in Fig. 4.4, we observed a linear trend and further performed the regression analysis. The statistical results show that the dissimilarities in two spaces are correlated significantly with $p < 0.005$. This validates the assumption and supports the Local matching scheme.

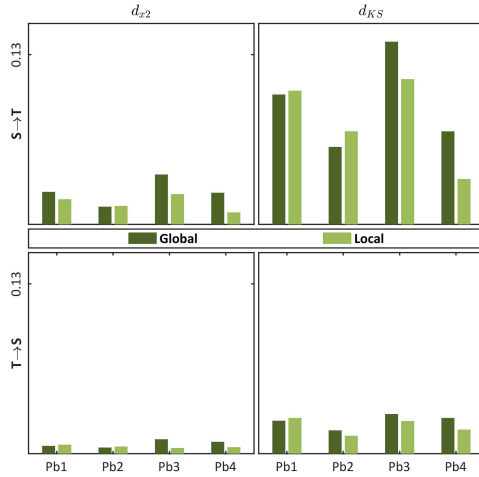


Figure 4.6: The bar chart of the distances for leave-one-out experiment for matching St.Jude to Terumo ($S \rightarrow T$) space and Terumo to St.Jude ($T \rightarrow S$) space. ‘Pb’ = ‘pullback’.

between matched and reference distributions for both Global and Local schemes are low and robust; see Fig. 4.6 and Table 4.2. The average distance of all four validation experiments (*Aver* in Table 4.2) indicates that, in general, the Local scheme outperforms the Global scheme.

Table 4.2: Results of leave-one-out cross validation

		S→T					T→S				
		Pb1	Pb2	Pb3	Pb4	<i>Aver</i> ^a	Pb1	Pb2	Pb3	Pb4	<i>Aver</i> ^a
d_{x2}	Global	.0248	.0135	.0381	.0241	.0251	.0058	.0046	.0110	.0090	.0076
	Local	.0192	.0141	.0231	.0091	.0164	.0069	.0053	.0042	.0049	.0053
d_{KS}	Global	.0994	.0593	.1398	.0711	.0924	.0252	.0179	.0303	.0273	.0252
	Local	.1022	.0724	.1110	.0347	.0801	.0276	.0137	.0246	.0183	.0210

^a The average performance of all the four leave-one-out experiments.

Scatter plots and Bland-Altman plots of the median intensities within ROIs are shown in Fig. 4.7. When comparing intensities in St.Jude space, an increasing trend is observed in the absolute systematic error; see Fig. 4.7(b,e,h,k). Following the conventional statistical procedure for Bland-Altman analysis [117], the St.Jude intensities were compared in the logarithm scale; see Fig. 4.7(c,f,i,l). Without an obvious trend in Terumo space, the intensities are compared in the linear space; see Fig. 4.7(a,d,g,j).

For the reference matching between the corresponding key frames, the systematic differences are -4.50 for $S \rightarrow T$ and 0.15 for $T \rightarrow S$; see Fig. 4.7(a,c).

Results of the leave-one-out validation for both St.Jude-to-Terumo ($S \rightarrow T$) and Terumo-to-St.Jude ($T \rightarrow S$) images are reported in Figs. 4.5, 4.6 and summarized in Table 4.2. For a section containing 70 images, generating the histograms takes 10 seconds. For the Local scheme, the time for searching in our database of 34 histograms using our Matlab (MathWorks, R2016a with Statistics and Machine Learning Toolbox) implementation is 1.25 seconds. Figure 4.5 shows the estimated target probability profile (normalized histogram) together with that determined by the aligned data (in red color; will be further referred to as the *aligned histogram*). The corresponding cumulative probability plots are shown as well. Both d_{x2} and d_{KS} are shown as bar charts in Fig. 4.6, and the numbers are reported in Table 4.2. The distances

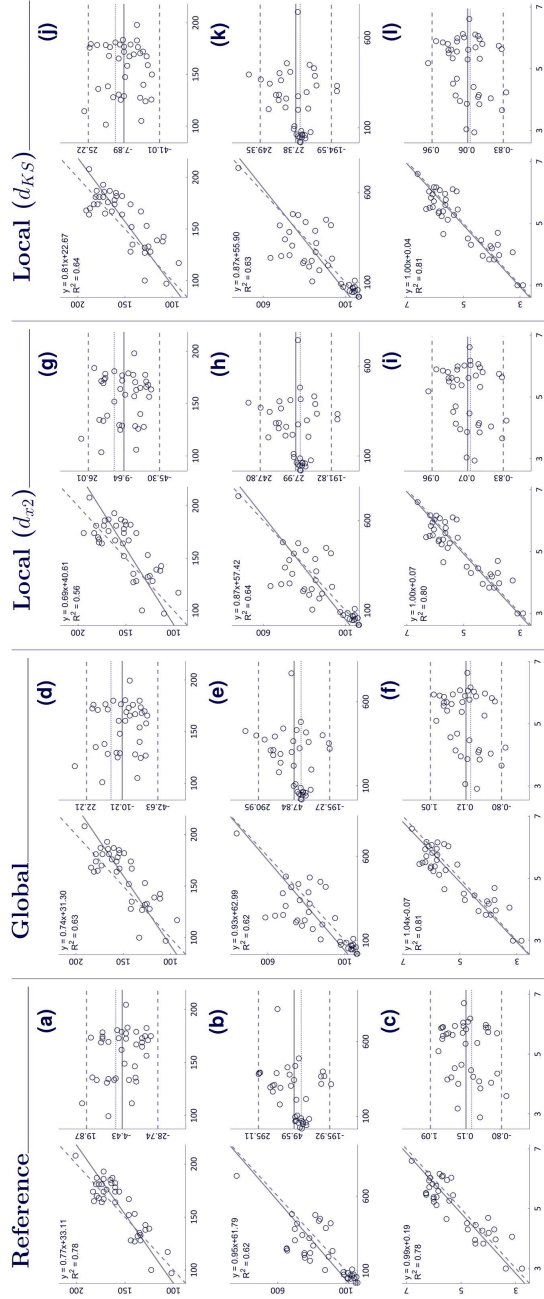


Figure 4.7: Scatter and Bland-Altman plots for comparing the median intensities within ROIs in target and matched frames ($n = 38$). Reference intensities, matched according to the aligned key frames (a,c), compared to that matched with the Global scheme (d,f), the Local scheme with d_{x2} (g,i) and the Local scheme with d_{KS} (j,l). In the scatter plots, the regression line is shown as the solid line and the dashed line indicates the $y = x$ line. In the Bland-Altman plots, the x -axis and the y -axis are the average and the difference of the target and matched intensities, respectively. The solid line indicates the average and the difference of the target and matched intensities, respectively. The dashed lines mark the 95% confidence interval. The matched intensities are compared in Terumo (a,d,g,i), St.Jude (b,e,h,k) and logarithmic St.Jude (c,f,i,l) spaces, respectively.

This difference is the most likely to be caused by the selection of data and is independent of the scheme used. Using this intrinsic systematic difference as a reference, the absolute systematic differences yielded by the Local scheme are relatively small: 9.67 (S→T) and 0.07 (T→S) for d_{x2} , 7.92 (S→T) and 0.06 (T→S) for d_{KS} , compared to the Global scheme: 10.26 (S→T), 0.12 (T→S). Taking into consideration the described intrinsic difference, the Local scheme yields absolute values closer to zero for both S→T and T→S matching. All comparisons in Bland-Altman analysis suggest that the Local scheme outperforms the Global scheme for EHS-based intensity transformation in IVOCT images between St.Jude and Terumo systems. The images matched with the target histogram determined by the Global scheme are shown in Fig. 4.8. The matched images, see Fig. 4.8(e–h,m–p), and the corresponding aligned images, see Fig. 4.8(a–d,i–l), show comparable intensity levels in both St.Jude and Terumo spaces.

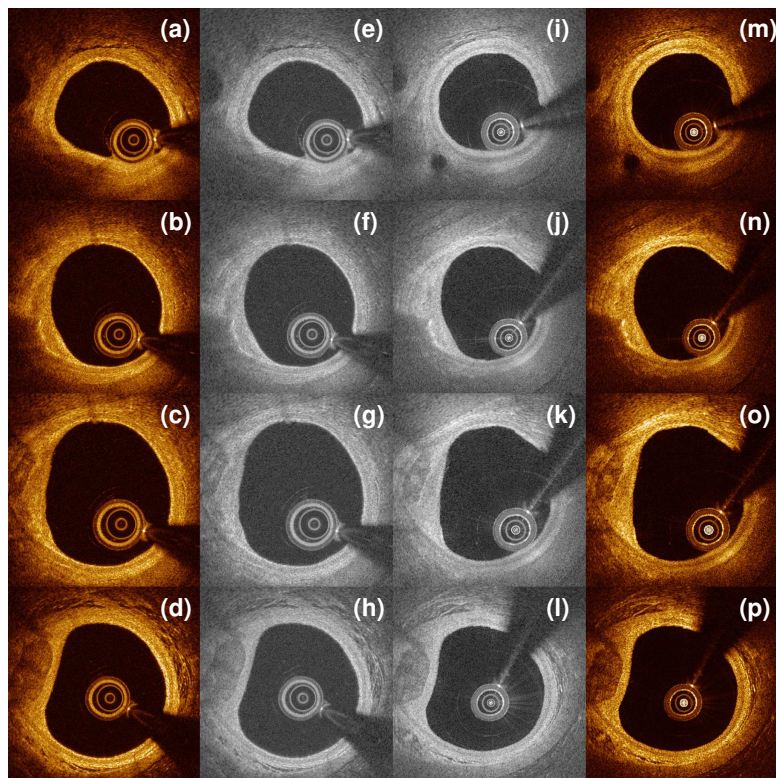


Figure 4.8: Images matched using the Global scheme. Raw St.Jude images (a–d) were mapped to the Terumo intensity space (e–h). Raw Terumo images (i–l) were mapped to the St.Jude intensity space (m–p). For visualization, St.Jude images are shown in its conventional golden color scheme.

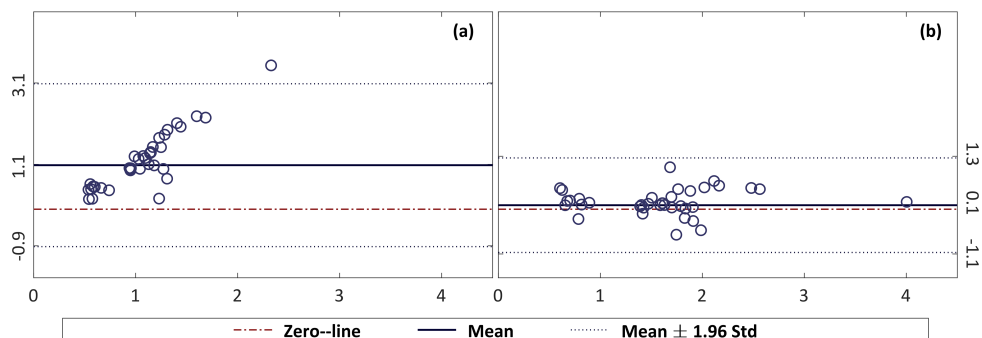


Figure 4.9: Bland-Altman plot of the comparison between estimated attenuation coefficients in ROI's in (matched/original) Terumo images and in corresponding ROI's in St.Jude images. (a) Attenuation values were estimated directly using original Terumo images. (b) The values were estimated using the Terumo images matched to St.Jude intensity space. Here 'Std' stands for 'standard deviation'.

4.5 Comparing attenuation coefficient values

One of the post-processing steps in IVOCT data analysis is estimation of the attenuation coefficients, which are defined as the distinction rate of light passing through a volume of tissue with a unit of μm^{-1} . It is considered to be a key feature for identification of different tissue types in the arterial wall. In our previous work [118], we reported the depth-resolved (DR) estimation using St.Jude images. However, applying this estimation directly to Terumo images results in values in different range. Therefore, we applied this estimation approach to the matched Terumo images (in St.Jude range) to validate the assumption that proposed matching scheme facilitates generalization of the attenuation estimation algorithm developed for St.Jude data to Terumo images. The results described above show comparable performance for both schemes. We further illustrate performance of the Global scheme for the estimation of attenuation coefficient using the DR method.

The attenuation was estimated both in the matched and original Terumo images. The median values within ROIs were compared to those estimated using St.Jude images. The paired t-test at 5% significance level was used with a null hypothesis that the mean difference between two sets is zero.

Figure 4.9 shows the Bland-Altman plots of the comparison of median attenuation coefficient in ROIs in (matched/original) Terumo images and in corresponding ROIs in St.Jude images. In the plot presented in Fig. 4.9a, original Terumo images were directly used for the estimation. Comparing to those estimated using the corresponding St.Jude images, the points are not evenly distributed around the zero-line, and both systematic difference and the range of random error are high. Paired t-test indicates that the mean difference is significantly different from zero with $p < 0.001$, and the 95% confidence interval (CI) is [0.74,1.42]. In Fig. 4.9b, the matched Terumo images were used

for the estimation. In this case, the difference with the values estimated using the St.Jude images is much smaller, which is indicated by lower systematic difference and random error range, and the points are more randomly distributed around the zero-line. For this case, paired t-test gives $p = 0.320$ with a 95% CI of [-0.10,0.30].

4.6 Discussion

Clinical significance of IVOCT structures has been reported extensively in clinical research. The use of IVOCT for the analysis of CADs grows exponentially. For more efficient analysis with minimum manual intervention, automated methods for tissue quantification, characterization, and classification are needed. However, lack of standardized image intensities can increase the difficulty of designing algorithms or restrict the possibility of generalization of algorithms developed for one specific imaging system. Therefore, standardizing image intensity is a crucial processing step to speed up the development and validation of methods for intravascular tissue analysis.

This study aims at exploring a proper scheme to match IVOCT image intensities with the local-mean EHS technique. In our case, the most essential step is to determine the target histogram. Preliminary statistical analysis suggests that distances in both spaces are significantly correlated. Based on this analysis, we propose a Local matching scheme and compare it with the Global scheme. Target histograms determined with both schemes turned out to be successful in matching IVOCT intensities at relatively low cost. In this, Local scheme marginally outperforms the Global scheme, which is in line with the results of our preliminary statistical analysis. Moreover, the attenuation estimation experiment presented in Section 4.5 illustrates benefits of using the Global scheme in practice by showing that it, in particular, largely improves the compatibility of the estimated attenuation coefficient across vendors.

Significant variation in the histograms of different sections is caused by many reasons, the difference in tissue composition being the major factor. As it has been reported in [8], tissue types are mainly visually assessed by recognizing bright speckle, presence of following shadow, sharpness of border, etc. Quantitative results confirm that these image structures yield variations in the histogram. Our previous study [90] demonstrated that image intensities can also be affected by position of the catheter. This effect can cause large variation in distances and thus can explain the low R^2 in the reported statistical analysis.

The Bland-Altman analysis shows a systematic difference in median intensities within selected regions of interest, even when the exact histogram is specified using the matched key frames. This intrinsic variation may be caused by many factors, such as the data alignment bias, intrinsic difference in systems for data acquisition, etc. Although this difference is relatively low, it should be accounted for in future applications of this method.

For clinical application, both schemes can also be easily embedded as an independent function for automated intensity standardization. For the global

scheme, the target histogram needs to be saved within the program. During calculation, this target histogram is loaded and used in EHS. For the local scheme, the database of histogram pairs needs to be saved. During calculation, the target histogram needs to be searched in the database and then it is used in EHS. Furthermore, the proposed experimental setup is not limited to the two considered IVOCT systems and can be used to standardize image intensities between other OCT systems or even for other modalities, e.g. MRI. Matching images to St.Jude or Terumo images can also further speed up the validation of newly developed IVOCT systems. As long as the order of intensities of different structures in both systems is consistent, strict ordering can be applied to insure that the exact histogram can be specified.

In this work we developed and presented a framework for minimizing intensity variation between two different IVOCT systems. At the same time, there might be variations caused by differences between systems from the same vendor, differences between catheters for the same imaging machine, and even differences in the pullbacks acquired using the same hardware and catheter. Since the images were calibrated by design during the acquisition, we expect these variations to be small.

Bare metal stents (BMS) were implanted in two out of the four pullbacks used in this particular study. Due to their high light reflectance, the BMS struts appear on the images as saturated bright spots with dark shadows behind them. They disturb the intensity distribution. Since this work mainly focused on matching images of the arterial tissue, images with stent struts were deliberately excluded from the analysis.

4.6.1 Limitation

The data used in this study is specially generated for construction of this intensity matching framework. Performing (virtually) simultaneous acquisition with two IVOCT systems is not done in clinical practice. Therefore, the amount of data used in this study is limited, which is a major limitation of this work. However, this data is unique and more representative for the analysis on intensity matching than *ex vivo* and animal data. Furthermore, results of leave-one-out validation show reasonable robustness through pullbacks and patients. At the same time, we acknowledge that extending the histogram database might potentially improve the histogram matching as using a larger database will most likely lead to more reliable estimation of the target histograms for both Global and Local schemes.

4.6.2 Future work

This histogram matching scheme will be used for standardization of IVOCT image intensities as a crucial first step for further quantification. Our future work will focus on comparing the outcome of existing quantification methods, such as attenuation estimation, quantification of the degradation of

bio-resolvable struts and differentiation of neointima, to data acquired by different IVOCT systems.

Once the matching framework is extensively validated, this approach can be routinely used as a pre-processing step for data standardization. The standardized images can be used for development of universal algorithms for segmentation (of e.g. fibrous cap of TCFAs) or tissue analysis (e.g. for estimation of attenuation coefficients).

In this study, we did not include the stented segments of the pullbacks due to the high reflectance of the metallic struts. However, for future work the database could be extended with the stented segments of the pullbacks by excluding individual strut points and their shadows from the images (rather than excluding the entire frame).

4.7 Conclusion

In this work, we presented our contribution to the construction of an intensity standardization framework for IVOCT images. We further contribute to the validation of two proposed schemes in the framework with data acquired by two of the most commonly used IVOCT systems in clinical research. Both local and global schemes are robust and produce accurate intensity matching. While local scheme performs marginally better than the global scheme, it requires a predefined histogram data set and is more time-consuming. Thus, for offline standardization of the images, the local scheme should be preferred for being more accurate. For online standardization or when another system is involved, the global scheme can be used as a simple and nearly-as-accurate alternative.